J Mater Sci (2009) 44:1219–1236
DOI 10.1007/s10853-008-3179-8

Moving finite-element mesh model for aiding spark plasma sintering in current control mode of pure ultrafine WC powder

G. Maizza · S. Grasso · Y. Sakka

Received: 18 December 2007 / Accepted: 9 December 2008 / Published online: 4 February 2009

Abstract The intricate bulk and contact multiphysics of spark plasma sintering (SPS) together with the involved non-linear materials' response make the process optimization very difficult both experimentally and computationally. The present work proposes an integrated experimental/numerical methodology, which simultaneously permits the developed SPS model to be reliably tested against experiments and to self-consistently estimate the overall set of unknown SPS contact resistances. Unique features of the proposed methodology are: (a) simulations and experiments are conducted in current control mode (SPS-CCm); (b) the SPS model couples electrothermal and displacement fields; (c) the contact multiphysics at the sliding punch/die interface is modeled during powder sintering using a moving mesh/moving boundary technique; (d) calibration and validation procedures employ both graphite compact and conductive WC powder samples. The unknown contact resistances are estimated iteratively by minimizing the deviation between predictions and on-line measurements (i.e., voltage, die surface temperature, and punch displacement) for three imposed currents (i.e., 1,900, 2,100, 2,700 A) and 20 MPa applied pressure. An excellent agreement is found between model predictions and measurements. The results show that the SPS bulk and contact multiphysics can be accurately reproduced during densification of ultrafine binderless WC powder. The results can be used to benchmark contact resistances in SPS systems applicable to graphite and conductive (WC) powder samples. The SPS bulk and contact multiphysics phenomena arising during sintering of ultrafine binderless WC powders are finally discussed. A direct correlation between sintering microstructure, sintering temperature, and heating rate is established. The developed self-consistent SPS model can be effective used as an aiding tool to design optimum SPS experiments, predict sintering microstructure, or benchmark SPS system hardware or performances.

Introduction

Despite the worldwide popularity of the SPS process, our capability to control sintering phenomena is still relatively poor. A number of physical microscopic and macroscopic mechanisms have been proposed to explain powder densification under the action of electric currents and pressure [1]. However, the common difficulty of measuring temperature in the sample makes the prediction of the final microstructure and its correlation with either sintering temperature or SPS parameters very difficult. As temperature measurements are only possible with an optical pyrometer at the outer die wall, and thermocouples suffer from an upper detection limit, alternative methods to interrelate actual sintering conditions with measured quantities are demanded.

Computer modeling is an effective aiding tool, in this respect, provided that the models are capable of capturing

G. Maizza (✉)
Dipartimento di Scienza dei Materiali ed Ingegneria Chimica, Politecnico di Torino, Corso Duca Abruzzi 24, Torino 10129, Italy
e-mail: Giovanni.maizza@polito.it

S. Grasso · Y. Sakka
Graduate School of Pure and Applied Sciences, University of Tsukuba, 1-1-1 Tennodai, Tsukuba 305-0047, Japan

S. Grasso · Y. Sakka
World Premier International Research Center Initiative (WPI Initiative) on Materials Nanoarchitronics (MANA) and Nano Ceramics Center, National Institute for Materials Science (NIMS), 1-2-1 Sengen, Tsukuba, Ibaraki 305-0047, Japan

the essential SPS multiphysics and their reliability is thoroughly tested against experiments. Among the available numerical techniques, the finite-element method is particularly suited for solving complex multiphysics problems with a strong non-linear materials' response.

Most of the published SPS macroscopic models refer to temperature control mode (SPS-TCm) experiments. It is well known that SPS-TCm operation mode utilizes closed currents loop feedback to indirectly control the sample's temperature by measuring the die wall surface temperature [2–15]. Most of the inherent SPS-TCm computer models, although suffice for qualitative SPS description, lack of prediction capability thereby are unable to reliably predict the sintering temperature or to correlate microstructure with SPS parameters. On the other hand, useful experimental information such as on-line voltage drop and punch displacement recordings are seldom used for this purpose although measurable and important to enhance models' reliability.

The aim of this paper is to illustrate a combined experimental/modeling methodology allowing building a reliable SPS model, which enables us to simulate actual SPS phenomena, including shrinkage-induced phenomena, and to self-consistently estimate the overall set of unknown SPS system contact resistances. The final aim is to quantitatively predict actual sintering conditions in the case of WC powder sample. Self-consistency is here referred to as the possibility of using the same SPS model in conjunction with designed SPS experiments to estimate a number of desired unknown SPS parameters. The designed calibration and validation procedures will enhance the accuracy of the model at each iteration by refining unknown parameters estimates. The convergence criterion is based on the minimization of the deviation between online recorded voltage, temperature, and displacements data and the corresponding computed field variables.

This paper is the second part of a wider research project aimed at investigating the SPS of ultrafine (UF) binderless WC powder with minimum grain growth. The first part is mainly focused on the experimental work and on the application of the designed methodology to establish a correlation between SPS parameters, sintering temperature, microstructure, and hardness in consolidated WC powder [16].

The paper's outline is as follows: the designed numerical/experimental methodology is described in Sect. The combined experimental/computational methodology; the features of the employed SPS apparatus and the conditions of SPS-CCm experiments are summarized in Sect. SPS current control mode (CCm) experiments; the SPS model is illustrated in Sect. The SPS model; the adopted solution strategy is illustrated in Sect. The solution strategy; the SPS model reliability and testing procedure are described in Sect. SPS model reliability; in Sect. Understanding of SPS multiphysics, the results are discussed and a new understanding of SPS is attempted; the main conclusions are drawn in Sect. Conclusions.

The combined experimental/computational methodology

The SPS process can be viewed as the result of a complex interplay between bulk and contact multiphysics, which may occur at the microscopic scale (i.e., particle level) as well as at the macroscopic scale (i.e., equipment level). A rigorous approach to SPS modeling should actually take into account phenomena at both scales. On the one hand, microscopic SPS and shrinkage phenomena can be accurately predicted provided that macroscopic electrothermal–displacement phenomena are reliably accounted. On the other hand, a macroscopic SPS model is reliable when a direct and intimate relationship between experiments and physical model is established.

Since quantitative predictions of macroscopic electrothermal along with shrinkage phenomena in SPS are not yet proved, the primarily aim here is to develop a methodology to accurately predict macroscopic SPS electrothermal phenomena occurring in the SPS system. The displacement field induced by powder shrinkage significantly affect heat generation and distribution inside the SPS system. Thus, it has to be taken into account in the SPS model although the presence of unknown experimental parameters inevitably introduces experimental and modeling difficulties.

The proposed strategy to approach the problem is to use the SPS model alternatively either as a parameter estimator or as an experiment designer. As new experimental data become available, the unknown SPS parameters estimate is refined, the model prediction capability improved and the designed experiments more effective. The basic requirement is that the SPS model is able to capture the essential features of the real SPS process.

Unique feature of the proposed methodology is that experiments and simulations are carried out under SPS-CCm rather than commonly used SPS-TCm. The SPS-CCm operation mode is here selected since it provides the simplest and most realistic method to compare SPS simulations with measurements.

This provides an effective criterion to experimentally calibrate and validate the developed SPS model and yet either to enhance understanding of the process or to speed-up the experimental setup. In addition, it suggests a convenient method to characterize intrinsic hardware features of SPS apparatuses, such as SPS contact resistances. Once the SPS apparatus is fully characterized with the help of the

SPS model, more complicated operation modes, such as SPS-TCm or SPS microscopic sintering phenomena, can be investigated.

As in SPS-CCm process, the imposed current is held constant until the measured punch displacement rate reaches steady state, the time to steady state in the punch displacement versus time curve defines the sintering time. Thus, for times greater than the sintering time only thermal effects are involved.

Another advantage of SPS-CCm is that higher and more controllable heating rates can be investigated. Indeed, heating rates of up to one order of magnitude greater than those in SPS-TCm are possible. High heating rates are particularly useful to control grain size in "difficult-to-sinter" ceramics powders, such as binderless UF WC powder, due to their sensitivity to rapid grain growth.

To enhance the reliability of the SPS model, several on-line readings, such as voltage, die surface temperature, and punch displacement, are exploited to calibrate and validate the SPS model.

To minimize experimental and computational efforts, the SPS model is kept as simple as possible but worth of capturing the essential bulk and contact multiphysics of the real SPS process. Bulk phenomena are assumed to be involved in graphite spacers, die, moving punch, and shrinking powder. The fundamental theory of resistive heating in bulk continuum media is well established and will not be discussed further. However, the "contact multiphysics" being less understood theoretically and experimentally will be presented in the contest of SPS. Several unknown factors such as non-smooth or contaminated surfaces, pressure, differential thermal expansion, relative sliding, etc. make the contact multiphysics between two surfaces very difficult to analyze.

In this work, special attention is given to contact resistance changes due to both differential thermal expansion phenomena and to relative sliding of contact surfaces during powder shrinkage. The unknown SPS contact resistances will be treated as lumping parameters and their estimate will be refined iteratively in function of temperature. The lumping parameters may embody others unknown factors, which are not explicitly taken into account by the model. The iteration process will converge to a final solution provided proper calibration and validation procedures are designed.

The porosity dependence of powder properties is taken into account through the on-line measured shrinkage versus time curve although a correction for the system differential thermal dilatation is required. The effective property approximation is assumed for the powder properties.

Figure 1 summarizes the basic principles behind the proposed methodology. It underlines that the final SPS model can be used to concurrently explore the actual process as well as to design optimum SPS experiments or to predict microstructure, once reliably calibrated and verified against experiments.

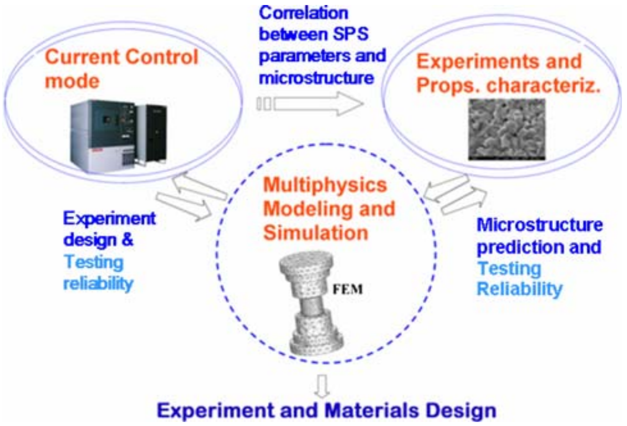

Fig. 1 Scheme of the proposed methodology based on SPS current control mode (CCm) experiments and simulations

SPS current control mode (CCm) experiments

In this section, only a brief overview on the experimental activity is given. Further details can be found in a preceding paper [16]. SPS experiments are conducted with a SPS-1050 (100 kN) machine (see Fig. 2 in [16]). The hollow cylinder die is made of graphite having 50 and 20 mm as diameters and 40-mm height. Two graphite foils are adopted to avoid possible interface reactions between the punches and the WC powder. All SPS experiments are carried out in vacuum under SPS-CCm with a constant uniaxial pressure of 20 MPa. Three imposed DC currents, say 1,900, 2,100, and 2,700 A are investigated. An optical pyrometer is employed to monitor the die surface temperature above 570 °C. The internal walls of the chamber are water cooled and held to a temperature of 25 °C. The influence of a graphite felt pan on radiation losses at the die surface is investigated. UF binderless WC powder is used as powder sample. Its average thickness is 2 mm after sintering (Fig. 2). A total number of 60 samples are processed to calibrate and validate the SPS model within the proposed methodology. Processing data along with inspected microstructures and measured hardness data are utilized to: (a) accurately estimate the SPS unknown set of contact resistances, (b) test the reliability of the developed SPS model; (c) assess the effectiveness of the overall methodology.

Figures 3, 4, 5 show the measured voltage, the die surface temperature and the punch displacement versus time profiles for the three investigated imposed currents,

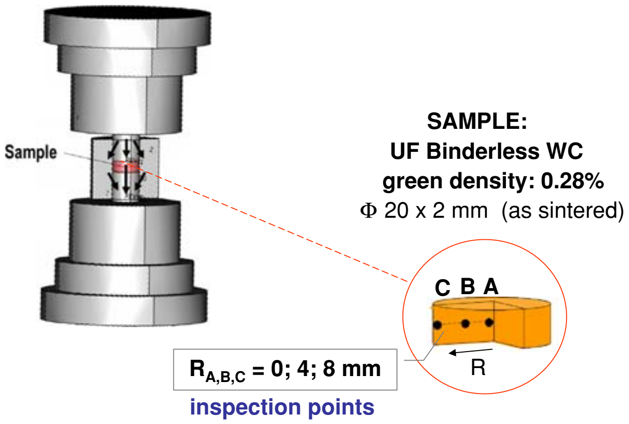

Fig. 2 Mechanical and microstructural inspection points in WC powder sample

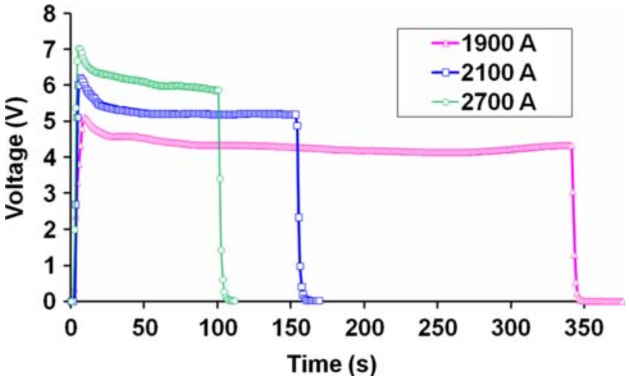

Fig. 3 On-line voltage drop measurement for 1,900, 2,100, and 2,700 A imposed currents and 20 MPa external pressure

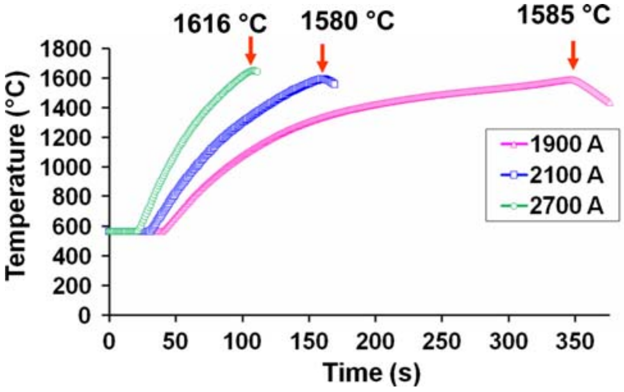

Fig. 4 On-line die surface temperature measurement for 1,900, 2,100, and 2,700 A imposed currents and 20 MPa external pressure; peak temperatures are also marked in

1,900, 2,100, and 2,700 A, respectively, and 20 MPa applied pressure. The peak temperatures and sintering times are, respectively, marked in Figs. 4, 5.

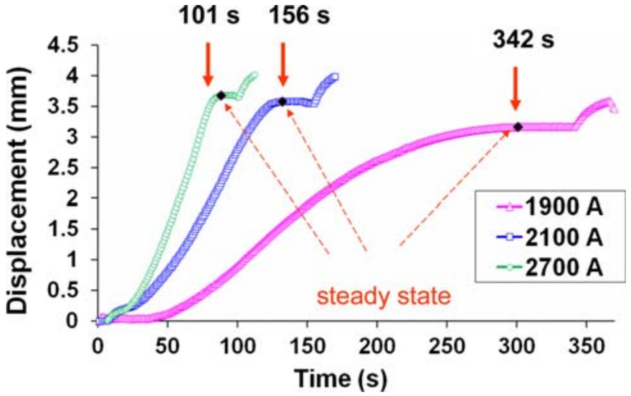

Fig. 5 On-line punch displacement measurement for 1,900, 2,100, and 2,700 A imposed currents and 20 MPa external pressure; sintering times are also marked in

The SPS model

The field coupling strategy

Electric and temperature fields are intrinsically coupled by Joule's effect both over the volume and at interface boundaries. A displacement field is associated to moving parts such as the upper spacer, punch, and powder. Such a displacement field can be computed by specifying a "true" shrinkage versus time function to the horizontal punch/powder interface using a moving mesh scheme. The computed displacement field may take into account thermal expansion effects (Fig. 6). Section Materials properties and the shrinkage model will illustrate the strategy how to extract the desired true shrinkage function from the measured punch displacement versus time curve.

Powder shrinkage affects the bulk electric and thermal fields via the change of powder physical properties (which in turn are function of porosity) and the contact resistances at punch/die, powder/die, and punch/powder interfaces. All these factors are described in detail in subsequent sections.

The electrothermal model

The accurate prediction of the influence of electric currents on the temperature field is crucial to control the SPS process. The current flow in graphite elements and powder is governed by the continuity equation, which follows from Maxwell's equations [17]:

$$\nabla\left[-\sigma(T,RD)_i\ \nabla U\right]=0 \tag{1}$$

with

$$\vec{E}=-\nabla U \tag{2}$$

and

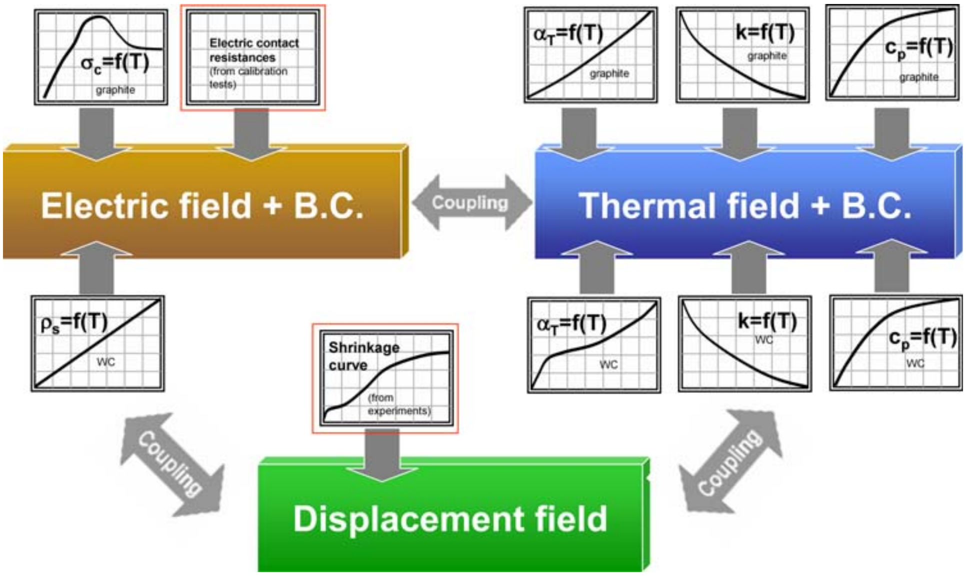

Fig. 6 Scheme of the SPS fields' coupling

$$\vec{J} = \sigma(T, \mathrm{RD})_i \vec{E} \tag{3}$$

where $\vec{J}$, $\vec{E}$, U, σ, and RD are current density vector, electric field vector, electric scalar potential, electrical conductivity, relative density, whereas subscript $i = 1$ stands for graphite element domains ($\mathrm{RD}_1 = 1$) and $i = 2$ stands for powder (RD_2 depends on the true shrinkage versus time function).

Joule heating is referred to as an irreversible phenomenon. It is a dissipative volumic heat generation ($\dot{Q}_V$) due to current flow resistance:

$$\int_{V_i} \dot{Q}_\mathrm{V}\, \mathrm{d}V = \int_{V_i} \vec{J} \cdot \vec{E}\, \mathrm{d}V = \int_{V_i} \sigma(T, \mathrm{RD})_i \left|\vec{E}\right|^2 \mathrm{d}V$$
$$= -\int_{V_i} \sigma(T, \mathrm{RD})_i (\nabla U)^2 \mathrm{d}V. \tag{4}$$

The heat generation term is coupled to Eq. 1 through the electrical conductivity. The latter depends on temperature and, in case of a powder domain, it is also function of displacement field through relative density. The heat generation term is also coupled to heat conduction equation which, in the integral form reads:

$$\int_{V_i} C(T, \mathrm{RD})_i \frac{\partial T}{\partial t}\, \mathrm{d}V = \int_{V_i} \nabla \cdot \left(k(T, \mathrm{RD})_i\, \nabla T\right) \mathrm{d}V$$
$$+ \int_{V_i} \dot{Q}_\mathrm{V}(T, \mathrm{RD}, U)_i\, \mathrm{d}V \tag{5}$$

where C, T, t, $\dot{Q}_\mathrm{V}$, are heat capacity, temperature, time, generated heat per unit volume V, respectively.

Equations 1–5 can be solved simultaneously in the system domain provided that initial conditions, boundary conditions, and interface conditions along with materials properties functions of temperature in both graphite and powder are defined. Due to the vertical axial symmetry of the arrangement, only half of it is computed.

Moving boundary and moving mesh model

To simplify the application and to highlight the advantage of the proposed methodology both experimentally and computationally, only the upper parts (i.e., spacer, punch, and powder sample) of the SPS system are assumed to move during sintering. This simplifying assumption permits to significantly reduce both the required computational time and the number of tested samples without considerably affecting the model accuracy and the generality of the final results.

The arbitrary Lagrangian–Eulerian (ALE) moving mesh technique [17] is employed to reproduce the axial displacement field change during sintering. Both spacer and punch move downwards during SPS according to a true shrinkage function $\delta(t)$ specified at the selected moving boundary (see Sect. Second-stage calibration: estimate of true shrinkage for evaluation of true shrinkage function). The upper horizontal punch/powder interface (Γ_3 in Fig. 7) is selected as prescribed moving boundary. The accurate specification of this interface is important to realistically reproduce actual contact areas change at both punch/die and powder/die (Γ_2, Γ_4 in Fig. 7) interfaces on sintering. It will be demonstrated as the latter are fundamental for the accurate estimation of electrical and thermal contact resistances (see Sect. SPS model reliability for details).

The ALE moving mesh is a built-in scheme in Comsol Multiphysics$^\mathrm{TM}$ package [17]. The moving boundary specification is combined with an efficient re-meshing technique to ensure the accurate prediction of unknown contact resistances and fields.

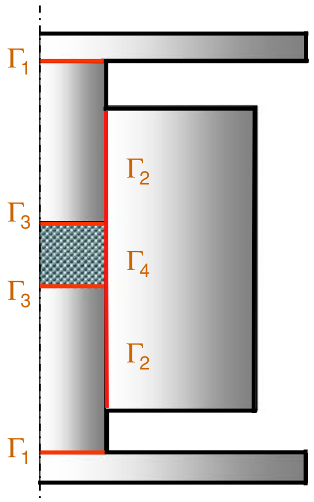

Fig. 7 Investigated SPS contact interfaces

Boundary conditions

In Fig. 8b, c, the electrical and thermal boundary conditions are summarized. A nil voltage is applied at the lower ram end, whereas a constant current is specified at the upper one. The lateral surfaces of graphite elements are assumed to be electrically insulated. A symmetry boundary condition is applied along the axial axis. Heat from graphite surfaces is mainly transferred to environment by radiation. Surface emissivity of graphite is assumed to be equal to 0.8 [18]. As the application of a carbon felt surrounding the die can significantly reduce radiation losses, experiments are conducted with and without graphite felt. As SPS process is commonly operated in vacuum (5 Pa), convection heat transfer can be reasonably ignored. The chamber walls as well as the upper and the lower ram surfaces are assumed to be at 25 °C all time. Adiabatic (or symmetry) boundary condition is assumed along the longitudinal axis.

Materials properties and the shrinkage model

The main advantage of assuming a microscopically heterogeneous material as macroscopically homogeneous is that the continuum field theory can be applied. This approach, however, requires the use of the effective property approximation to evaluate the physical property functions in graphite and powder domains. Heat capacity, thermal expansion, electrical, and thermal conductivity are all assumed to be functions of temperature. In the powder domain, the time dependence on relative density is also taken into account. During SPS, the porous domain evolves from a very loose condition (RD ~ 0.28) to almost a full density condition, passing through various degrees of porosity. Several empirical or semi-empirical relations are available in the literature to correlate thermal and electrical conductivity directly to porosity (or relative density) [18–20]. These relations, however, cannot apply when relative density is lower than 50%. One of the simplest

Fig. 8 Assumed SPS model's boundary conditions:
a displacement; **b** electric field;
c thermal field

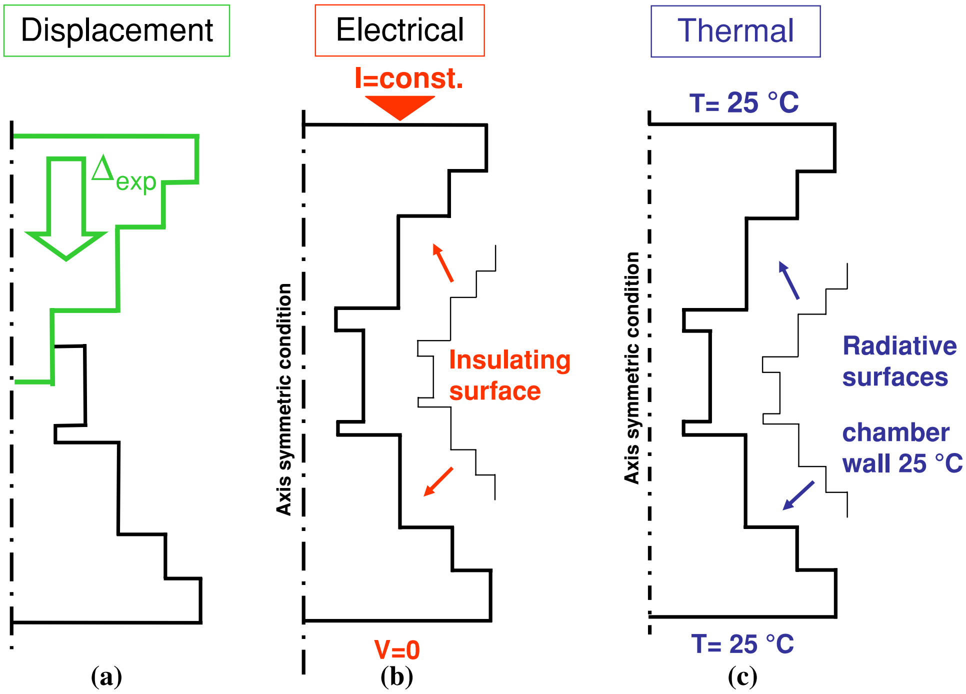

relations is that proposed by Sahimi et al. [21]. For electrical and thermal conductivity, this relation reads:

$$\sigma/\sigma_b = \mathrm{RD} \quad k/k_b = \mathrm{RD}. \tag{6a, b}$$

Equation 6a, b assumes a macroscopically homogeneous isotropic medium. In a microscopically heterogeneous medium, however, the properties are expected to vary from point to point.

At any time, the instantaneous relative density and the compact shrinkage $\delta(t)$ have to fulfill volume conservation:

$$\frac{\mathrm{RD}(t)}{\rho_0} = \frac{V_0}{V(t)} = \frac{\delta_0}{\delta(t)} \tag{7}$$

where V is volume and "0" stands for initial condition. In Eq. 7, the relative density works as a coupling parameter between electric, thermal, and displacement field. The measured punch displacement $\Delta_{\exp}(t)$ provides a convenient measure of the true shrinkage provided that it is corrected for thermal expansion effects (see Sect. First stage of calibration: evaluation of expansion effects in graphite for details).

The temperature dependence of electrical and thermophysical properties are taken from reference [22, 23] except for graphite GS-203 properties [24].

The contact resistance model

When two materials are pressed together, the relative contact may be attained at finite number of points. The electrical and thermal contact resistances depend on several factors [25–31]: (a) surface finish/cleanliness of contacting materials; (b) nature and morphology of materials in contact; (c) applied pressure; (d) interface temperatures (significantly affected by constriction and surface effects); (e) contact surface area [23, 25]. Note that while the contact pressure can play a significant role, especially when a non-intimate contact is established between two contacting surfaces, the interface temperature is always an important factor in establishing the contact conditions as itself may affect the contact pressure too. Applied pressure also affects the contact resistance [27].

Across a perfect interface, the temperature and the electric potential are usually continuous functions. However, the presence of geometric irregularities may prevent a perfect contact.

In the SPS apparatus, the contact surfaces act in vacuum under the influence of an external uniaxial pressure. Figure 7 shows the various contact interfaces of interest in the SPS system. The contact interfaces may broadly be classified into either homogeneous (graphite/graphite) or heterogeneous (graphite/powder) interfaces.

Prior studies mainly focused on the vertical contact resistance clearly show that the vertical interfaces are more sensitive to sintering conditions than horizontal ones, although the general behavior of heterogeneous interfaces remains obscure. Because contact resistances change during sintering, it is not a priori possible to predict the electric current distribution across such interfaces. Due to this lack of physical knowledge, it has been decided to model the overall SPS contact resistance system. Figures 9, 10 depict the basic principles of SPS contact resistance changes during sintering. These principles have been incorporated into the SPS model by means of the moving mesh technique. The horizontal contact resistance R_1 (at Γ_1 interface) is treated separately. This contact resistance is characterized by a severe constriction effect resulting from the large ratio of spacer to punch surface areas. From modeling standpoint, constrictions phenomena are modeled by Eq. 1. However, to completely determine R_1, the support of specific experiments is required to account for any accidental factor, which can arise in most contact interfaces during service operations such as wear, contamination, heating/cooling degradation, etc. According to Figs. 9, 10, the contact resistance R_2 exhibits two important features: (a) the two contact surfaces relatively slide along the longitudinal axis undergoing large displacements and (b) the involved contact area is largest in the SPS system. The relative movement of the contact surfaces is here modeled by a combined moving boundary/moving mesh technique since it can manage relatively large sintering displacements. The (b) feature underlines that even slight changes in R_2 may dramatically affect the SPS system behavior.

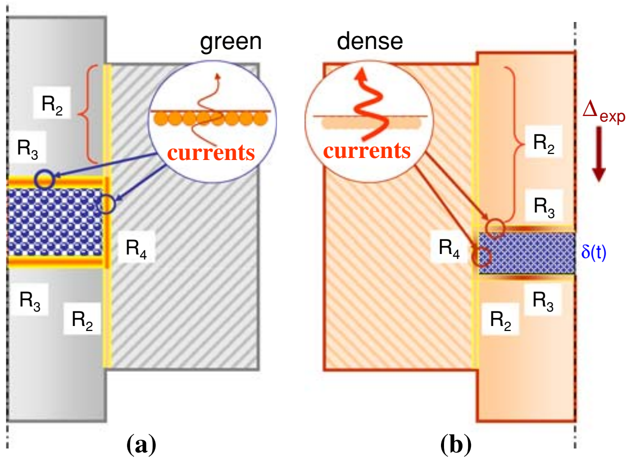

Fig. 9 Transient phenomena associated to major SPS contact resistances: **a** initial system configuration: contact resistances are largest due to green powder (R_3, R_4) and minimum contact area (R_2); **b** intermediate system configuration: contact resistances decrease due to denser powder (R_3, R_4) and increased contact area (R_2)

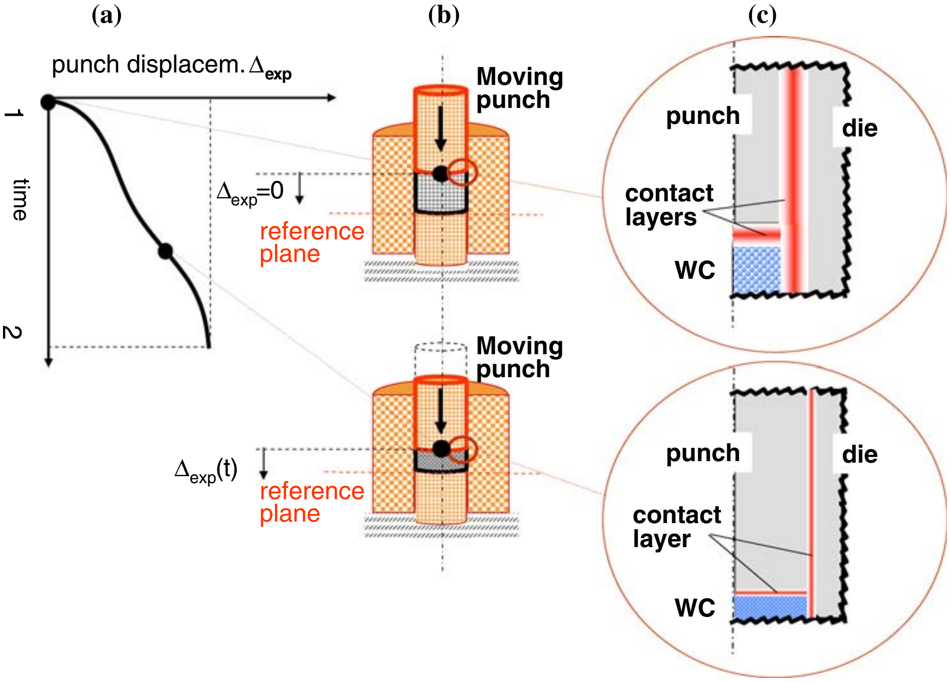

Fig. 10 Working principle of the moving mesh/moving boundary technique to model the change of R_2, R_3, and R_4 contact resistances during sintering: **a** measured punch displacement curve; **b** imposed true punch/powder displacement (moving boundary) driving the moving mesh within the upper spacer/punch/powder assembly; **c** contact resistance change due to powder shrinkage: the thicker the interface, the larger the contact resistance

This implies that special care has to be taken in modeling R_2 phenomena. R_4 is crucial because it involves a contact with a powder surface, which shrinks during sintering. In the present continuum approximation, this surface shrinks according to a specified true shrinkage law. A large change is also expected for R_4 especially at early sintering times, due to the very low initial green density (about 28% relative density) of the powder sample. The contact resistance R_3 is modeled through the time dependence of relative density (RD) on electrical and thermal properties of the powder compact.

Computationally, the whole set of contact resistances R_i is implemented in the program by interposing a thin layer between the two contact surfaces of unknown film resistance. This layer may take an arbitrary thickness (t) but actual contact area. The electric current density and the thermal flux across the interface are given by:

$$J_c = \sigma_c(U_1 - U_2) \quad \dot{q}_c = h_c(T_1 - T_2) \tag{8}$$

where c denotes contact interface, 1 and 2 identify the individual contact surfaces and $\dot{q}_c$, σ, and h are thermal flux across the interface and the electric and thermal gap conductances, respectively. Joule-effect dissipation at an interface can be modeled as:

$$\dot{q}_c = J_c(U_1 - U_2) = \sigma_c\,(U_1 - U_2)^2. \tag{9}$$

According to Holm theory [25], the electric contact resistance R_c for a homogeneous interface depends on contact area (or pressure) and local temperature. The latter, in turn, influences the local physical and mechanical properties as:

$$R_c = \frac{\rho_s(T)}{2\,a(t)} \tag{10}$$

where ρ_s, a are electrical resistivity and radius of the contact area between two bodies, respectively. For a heterogeneous interface, the electric contact resistance reads:

$$R_c = \frac{\rho_{s,1} + \rho_{s,2}}{4\,a(t)} \tag{11}$$

where $\rho_{s,1}$ and $\rho_{s,2}$ are electrical resistivities of the two materials.

Equation 10 gives a tangible evidence of the multi-physics nature of contact phenomena in SPS. The electrical resistivity depends on temperature; the contact surface radius is related to the true displacement (i.e., shrinkage) function and indirectly related to applied pressure. Due to the large change of contact area, large changes in the electric and thermal fields are also expected across the inherent interfaces.

Simulation works [8, 10] report the estimates of the electrical gap conductance by assuming for the electrical and thermal gap conductance the same temperature dependence as assumed for bulk properties. In addition, they assume that the overall SPS contact resistance system can be accounted by only two parameters, namely the horizontal and the vertical contact resistance, respectively, for either the electrical and thermal contact conductances (or resistances).

In addition, contact resistances may be additionally affected by differential thermal expansion. Especially, the radial thermal expansion may cause the vertical contact pairs to become tighter during sintering. This may imply a significant change in the electric and heat generation and distribution. On the other hand, the axial thermal expansion may affect the shrinkage phenomena with direct consequences on horizontal contact pairs.

The electric and thermal film resistances are expressed as:

$$R_i/t = 1/(\sigma_i A_i) \quad K_i/t = 1/(k_i A_i) \qquad (12\mathrm{a,b})$$

where σ_i and k_i are electrical and thermal conductivities, respectively, and i is the ith contact pair.

Equations 6a, b are entered in the SPS model as interface conditions. Despite literature works [8, 10], constant electric and thermal film resistances [8] are assumed only at the beginning of the iteration process (initial guesses). Since our primary purpose is to reliably reproduce electric and thermal effects during SPS a suitable temperature function is assumed for all R_i, other than the time function.

The relative kinematics of contact surfaces is controlled by the moving mesh technique taking into account Eq. 7, as described in detail in Sect. Moving boundary and moving mesh model. The effect of increased pressure due to thermal expansion on horizontal resistances (R_1, R_3), though incorporable in the actual shrinkage function $\delta(t)$, can be ignored in comparison to vertical contact resistances (R_2, R_4) since the latter depend on the much larger and constant imposed pressure. Instead, the radial differential thermal expansion at the punch/die interface will also affect the vertical contact resistances as detailed in Sect. SPS model reliability. Thus, only the temperature dependence of R_i parameters is needed to be estimated by systematic modeling and experiments being any other unknown factor automatically included as lumping factors in the R_i estimates (see Sect. First-stage calibration: estimation of homogenous contact resistances for details).

Initial conditions

In SPS-CCm process, a constant current (i.e., either 1,900, 2,100, or 2,700 A) is initially imposed and held constant until the on-line recorded punch displacement reaches steady state. At the start of simulation, the temperature field is set to room temperature everywhere. The initial porosity of the powder is 28%. The moving (upper) punch/spacer assembly is initially in the topmost position (Fig. 8a).

The solution strategy

The overall set of SPS governing equations along with initial conditions and boundary constraints are solved using a commercial finite-element package [17].

Maxwell's equation (Eq. 1) and the energy balance equation (Eq. 5) are simultaneously solved with inherent coupling terms.

SPS-CCm experiments and simulations are carried out using three imposed currents (i.e., 1,900, 2,100, and 2,700 A) at the constant pressure of 20 MPa. Currents and pressure are selected among those insuring full density of WC powder during actual experiments. Specifically, 2,100 and 2,700 A are used for model calibration and 1,900 A is used for model validation.

Completion of SPS experiments is assumed to occur when the recorded punch displacement reaches steady state (Fig. 5).

In the model, the upper punch/powder interface (Γ_3) is assumed to move according to a specified $\delta(t)$ "true" shrinkage, meaning that it is corrected for system thermal dilatations. Because the moving boundary describes the real punch relative sliding it will also describe the actual transient changes of the system contact resistance with related induced electric and thermal fields. The mesh in the powder and punch regions is coarse initially. Typical mesh configurations, e.g., at the initial and final stage of sintering, are reported elsewhere [16]. The mesh is denser along the contact interfaces to assure higher accuracy in the estimate of unknown parameters.

All materials properties are assumed as functions of temperature and, in case of the powder region, also of relative density (Eq. 7).

SPS model reliability

To be reliable, the developed SPS model has to be thoroughly tested against experiments. These are designed to estimate unknown SPS parameters, such as contact resistances and thermal expansion effects. According to the calibration methodology, any effect or phenomena induced by or caused during service or working operations, such as wear, oxidation, or degradation between contact surfaces as well as changes in the initial powder conditions, etc., not specifically accounted in the SPS model, will be automatically incorporated in the contact resistance estimates. However, the estimation process may provide inconsistent results if the contact surfaces experience excessive degradation during the calibration and validation procedure. To minimize this inconvenience, the overall number of samples to be processed should be not so high, though enough to give reliable estimates. Here, 60 samples are selected as a good compromise between accuracy and process reproducibility.

After sintering the WC samples are inspected morphologically by SEM and mechanically by Vickers indentation test. More details on the final correlation between microstructure, hardness, and sintering temperature are given elsewhere [16].

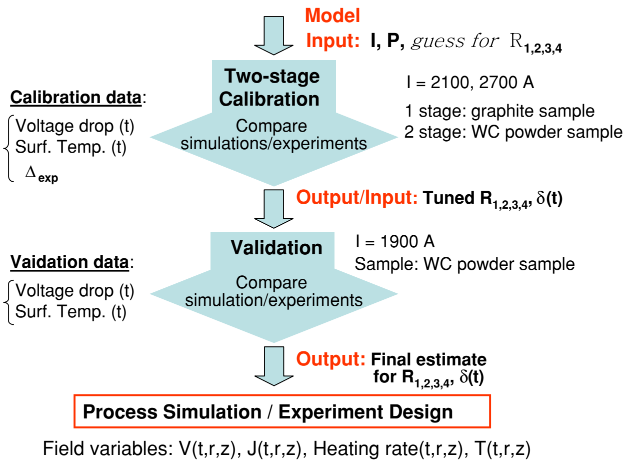

Fig. 11 Flow diagram for SPS model calibration and validation

Figure 11 summarizes the flow of both the calibration and validation procedures. The following sections illustrate in detail these two procedures.

The calibration procedure

The overall calibration procedure is conveniently split into two parts using 2,100 and 2,700 A. Each part includes two stages. The first stage is addressed to evaluation of SPS system features in the absence of powder. That is only graphite samples are tested. Temperature and voltage drop measurements are used to evaluate the contact resistance versus temperature (e.g., R_1, R_2) functions of homogeneous (graphite/graphite) interfaces. The second stage is addressed to evaluation of combined effects of graphite equipment parts with WC powder sample. In the second stage, temperature and voltage drop measurements are used to estimate the two major heterogeneous (graphite/WC) contact resistance (R_4, R_3) versus temperature functions, while R_2 estimate is refined, taking into account the presence of WC powder. Since WC powder involves shrinkage phenomena as well as differential thermal expansion, these effects are then analyzed by combining both, first and second stages of calibration. The effect due to the presence/absence of an insulation carbon felt surrounding the die surface is also taken into account in the first part calibration. The model accounts for the use of felt by reducing of 0.3 factor, the standard graphite relative emissivity (i.e., 0.8). This factor is estimated by specific calibration tests, by alternating experiments and simulations with and without felt.

First-stage calibration: estimation of homogeneous contact resistances

The graphite die is filled with a graphite disk (Φ 20 mm, *t* 7 mm) to estimate R_1 and R_2 homogeneous contact resistances. Simulations are initialized with four constant contact resistance guesses for both the electric (σ) and thermal (h) film conductances [8, 10]:

$$\sigma^{\mathrm{H}}_{\mathrm{g/g}} = 1.25 \cdot 10^{7} (\Omega\,\mathrm{m}^2)^{-1}, \quad \sigma^{\mathrm{V}}_{\mathrm{g/g}} = 7.5 \cdot 10^{6} (\Omega\,\mathrm{m}^2)^{-1} \tag{13a, b}$$

$$h^{\mathrm{H}}_{\mathrm{g/g}} = 2.2 \cdot 10^{3} (\mathrm{W/m^2\,K}), \quad h^{\mathrm{V}}_{\mathrm{g/g}} = 1.32 \cdot 10^{3} (\mathrm{W/m^2\,K}) \tag{14a, b}$$

where H and V stand for horizontal and vertical interfaces, respectively, and g/g denotes graphite/graphite interface. In doing so, all horizontal (R_1 and R_3 with K_1 and K_3) and all vertical (R_2 and R_4 with K_2 and K_4) film resistances take the same initial value.

Through systematic coupling of experiments and simulations, the contact resistance values are iteratively refined. First, the electric film resistances are refined by fitting the recorded and predicted voltages. Secondly, the thermal film resistances are refined by fitting the recorded and predicted temperatures at the outer die surface. In the calibration process, each contact resistance versus temperature function is built point-wise. As these temperature functions are refined, the SPS model becomes more reliable. The eight best-fitting values of the homogeneous electric and thermal contact resistances are finally computed for 2,100 and 2,700 A, with and without insulation felt.

Figures 12a–f compare voltage and temperature results after the first-stage calibration for 2,100 and 2,700 A, with and without the effect of insulation felt. Note that the SPS cooling period, that is for times longer than the sintering time, is not simulated.

Specifically, Fig. 12a, c compare computed and measured voltage histories for two currents (2,100 and 2,700 A) without insulation felt. Figure 12b compares computed and measured voltage histories for the same current (2,100 A) with insulation felt. Analogously, Fig. 12d–f show the corresponding computed and measured temperature histories under the same operating conditions of Fig. 12a–c. The minimum detection limit of 570 °C for the employed pyrometer impedes to plot experimental temperatures below this value. In Fig. 12d–f, the predicted peak temperatures are 1,474, 1,645, and 1,505 °C, after 185, 132, and 102 s sintering times, respectively. Thus, the higher is the imposed current, the shorter is the sintering time. The SPS operation without the insulation felt leads to a peak temperature of 171 °C lower, or a heating time of 53 s longer, than those with felt, for 2,100 A.

The abrupt voltage drop observed at longer times in Fig. 12a–c, identifies the shutdown of power supply. Instead, the slight voltage drop observed in the first stage of heating is attributed to the rapid increase of the contact

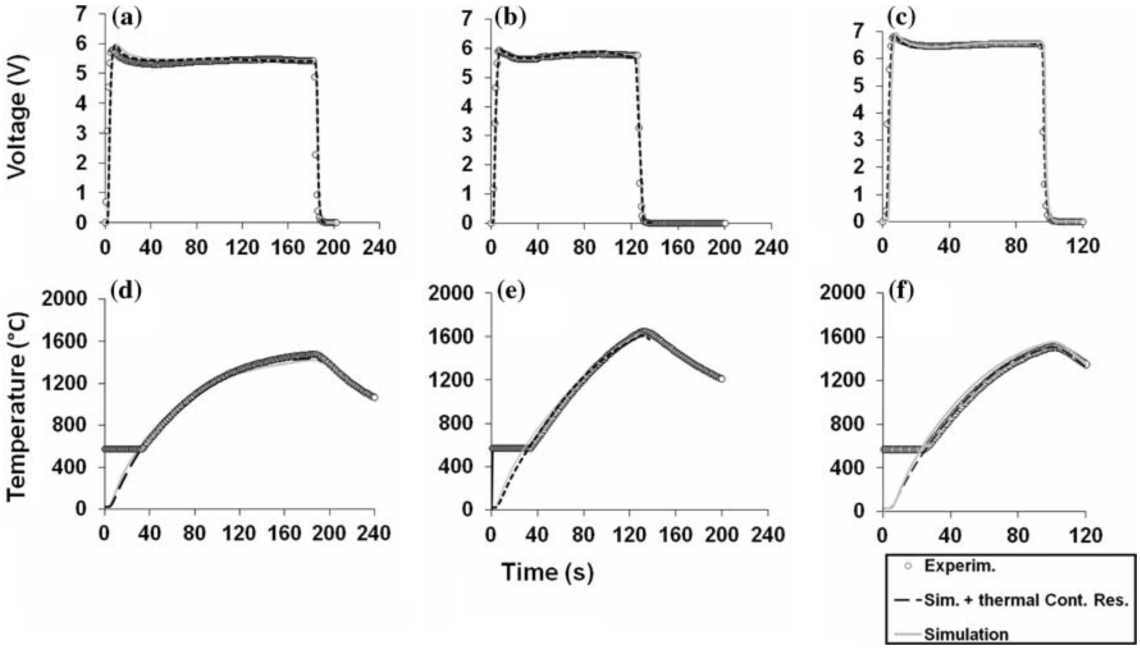

Fig. 12 Predicted and measured time profiles of voltage (**a**, **b**, **c**) and die surface temperature (**d**, **e**, **f**) in case of graphite compact for 2,100 A and (**a**, **d**) without felt; for 2,100 A with felt (**b**, **e**); for 2,700 A without felt (**c, f**). T.C.R. denotes the effect of thermal contact resistance in the best-fitting iteration procedure

resistance during the system start-up. The highly localized heat at interfaces explains the rapid system heating in the initial transient. The agreement between simulations and experiments is satisfactory in all cases. A closer fitting between simulations and experiments is often achieved when the effect of unknown thermal contact resistances (T.C.R.) is also taken into account in the iteration process.

First-stage of calibration: evaluation of expansion effects in graphite

The differential thermal expansion along the radial direction exerts a strong influence on the vertical contact resistances during sintering. The resulting increased contact pressure causes the conductance at the punch/die interface also to increase which, in turn, influences the powder shrinkage phenomena through the change of electric field, heat generation, and temperature field. As a result, thermal expansion phenomena significantly influence heating rates. In SPS-CCm process, on the other hand, heating rate increases with increasing imposed current. This relationship provides a useful means to evaluate thermal expansion effects along the radial direction as illustrated below.

A number of specific experiments are required to analyze the contact resistance change as a function of imposed current. The results show that the contact resistance increases with increase in temperature for low imposed currents, whereas it does not change significantly for high imposed currents (e.g., 2,700 A). Thermal expansion plays a role also along the axial direction. Its evaluation is important to estimate the true shrinkage $\delta(t)$ having the recorded punch displacement $\Delta_{\mathrm{exp}}(t)$ data. The true shrinkage can be defined as:

$$\delta(t) = \Delta_{\mathrm{exp}}(t) - \delta_{\mathrm{T}}(t) \qquad (15)$$

where $\delta_T(t)$ is the axial (differential) thermal expansion term. The estimation of this term is not trivial and requires a special purpose calibration procedure with both graphite and WC powder samples.

The contribution of thermal expansion effect with graphite sample is first discussed. For convenience, in Fig. 13, this contribution is shown together with that obtained using the WC powder sample. The latter is discussed in the second stage of calibration for consistency. Figure 14 is also useful for reference, which shows the measured thermal expansion of the system in function of die surface temperature for 2,100 and 2,700 A with insulation felt. These curves are used to comparatively assess the thermal expansion effects, for the two imposed currents, as well as to evaluate heating rate effects on sintering. However, to this purpose, further information are required. These are collected from the second-stage calibration, as illustrated in next section.

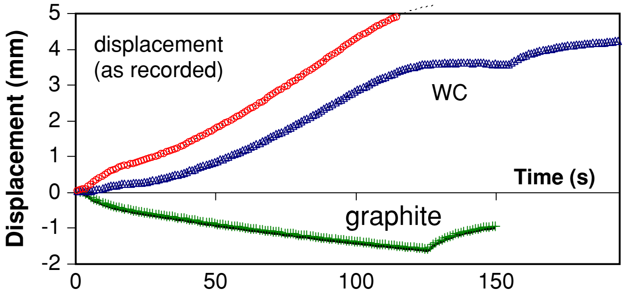

Fig. 13 Punch displacement (as recorded) and thermal expansion curves in case of graphite compact (measured) and WC powder (measured) for 2,100 A. These curves are utilized to estimate the true shrinkage

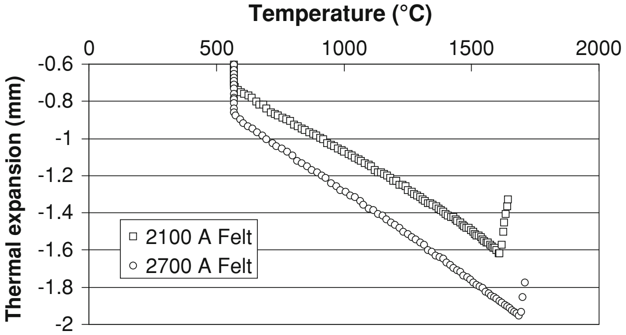

Fig. 14 Measured thermal expansion versus die surface temperature in case of graphite compact and insulation felt for 2,100 and 2,700 A

Second-stage calibration: estimate of true shrinkage

Figure 13 shows the measured displacement for 2,100 A, using graphite sample (first-stage calibration) and WC powder (second-stage calibration). This curve permits to estimate the true shrinkage $\delta(t)$ according to Eq. 15. The estimated $\delta(t)$ function is entered in the validated SPS model to reliably reproduce the actual punch relative sliding with inherent electric and temperature fields.

Second-stage calibration: estimate of heterogeneous contact resistances

In this stage, a WC powder disk (Φ 20 mm, t 7 mm) is filled in the die. The two major heterogeneous (graphite/WC) electric contact resistances (R_3, R_4) are first estimated versus temperature. At the same time, the previously estimated R_1 and R_2 are refined. The film resistances as estimated in the first stage are entered in the model as initial guesses.

The experimental/modeling tuning procedure follows that of first stage. The heterogeneous thermal contact resistances are thus estimated and refined. The iteration process progressively converges to an optimum solution since the agreement between predictions and experiments steadily improves.

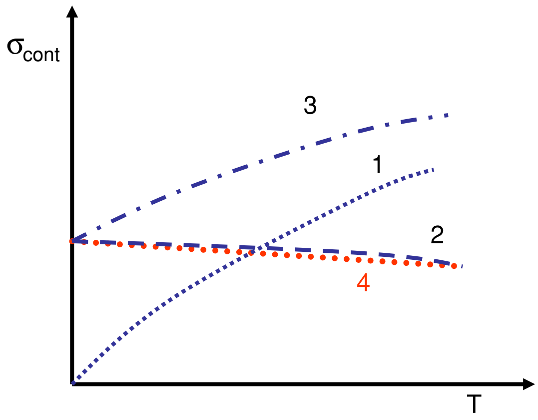

Fig. 15 Qualitative behavior of contact conductances versus temperature as estimated after first- and second-stage calibration

A qualitative behavior of the estimated conductance functions is shown in Fig. 15. Note that these estimates are specific of the employed SPS hardware and operating conditions. It is peculiar that the contact conductances σ_1 and σ_3 (Eq. 12a, b) are found to increase with increasing temperature, whereas σ_2 and σ_4 are decreasing function. The latter behavior is not obvious, since it comes from an iterative experimental/numerical refinement process according to the proposed methodology.

The subsequent results are best appreciated comparatively against those obtained with graphite sample in the first stage.

Figure 16 shows the measured total (i.e., bulk + contact) electric resistance during heating for 2,100 and 2,700 A, respectively. It shows that regardless the kind of sample used, the lower imposed current the higher the total resistance. The total resistance is generally very high at the early transient. It rapidly attains a maximum peak, then it decreases until a quasi-steady state value is achieved. Such resistance peak is more pronounced in WC powder at low imposed currents. The maximum resistance peak can be attributed to the initially dominant vertical (R_2, R_4) contact resistance and their subsequent sudden decrease due to punch sliding (i.e., powder shrinkage).

The sliding punch exhibits highest resistivity initially. While moving, however, it reduces its contact resistance (R_2) as its contact area (with the die) increases. Subsequently, the punch (and compact) bulk resistance start to decrease during sintering. This reasoning is supported by measurements of temperature (Fig. 17) and voltage drop (Fig. 18) profiles, which show the measured temperature and voltage, respectively, for 2,100 A using either graphite

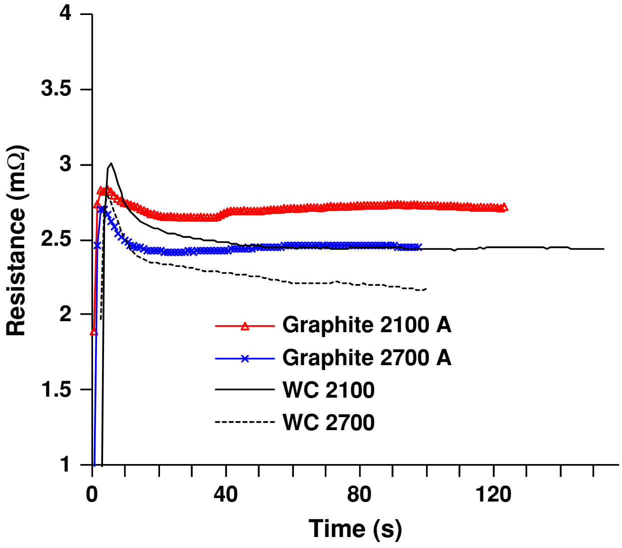

Fig. 16 Measured total (bulk + contact) electric resistance versus time, for 2,100 and 2,700 A, in case of either graphite compact or WC powder

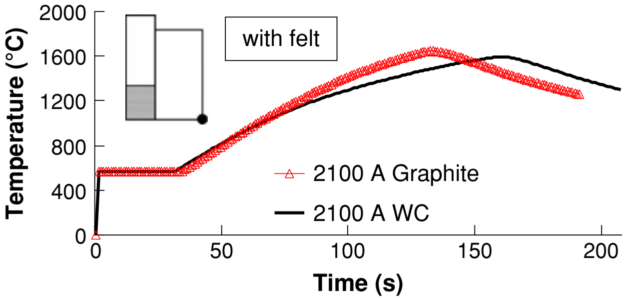

Fig. 17 Measured die surface temperature versus time for 2,100 A, in case of either graphite compact or WC powder, with insulation felt

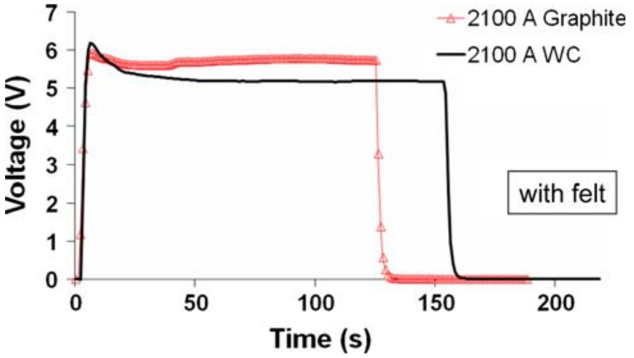

Fig. 18 Measured voltage versus time for 2,100 A in case of either graphite compact or WC powder, with insulation felt

or WC powder as a sample. Remind that in graphite sample no densification exists, thereby only thermal expansion is involved. The total electric resistance is generally higher with graphite sample in the absence of punch sliding. The temperature peak of graphite is higher than that of WC powder since a motionless punch involves a higher resistance or a more severe heat generation compared to shrinking WC powder. The total electric resistance decreases with increasing imposed current probably because of the direct influence of currents on the contact resistances and/or because of the involved different temperature field which, in turn, affects the system heating. The large difference in the two temperature profiles (Fig. 17) can be indeed, a reason for the different behavior of graphite and WC powder samples. Figures 17, 18 confirm that graphite sample is heated faster than WC powder and that the initial steeper voltage drop in the latter results from its densification.

The validation procedure

The validation procedure serves two basic objectives: (a) assess the reliability and the prediction capability of the calibrated SPS model (b) prove the reliability of the overall methodology.

The first objective is achieved by applying the SPS model to simulate a SPS process with WC powder sample under new operating conditions other than those used for calibration. No parameter adjustment is allowed in this stage. The resulting simulations and experimental results are checked to be within a desired tolerance. To this purpose, a 1,900 A imposed current is selected.

The results are shown collectively in Figs. 19, 20 for 2,100 and 2,700 A (calibration) and 1,900 A (validation) conditions. These figures compare predicted and experimental voltages and temperatures, respectively. As can be seen, the agreement is very good including the case of lower imposed current of 1,900 A.

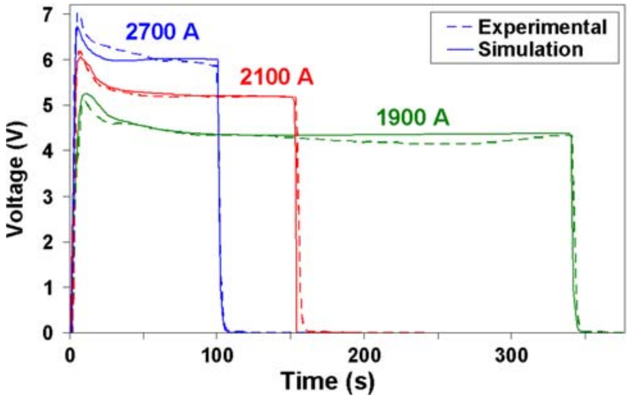

Fig. 19 Measured and predicted voltage versus time for 1,900, 2,100, and 2,700 A

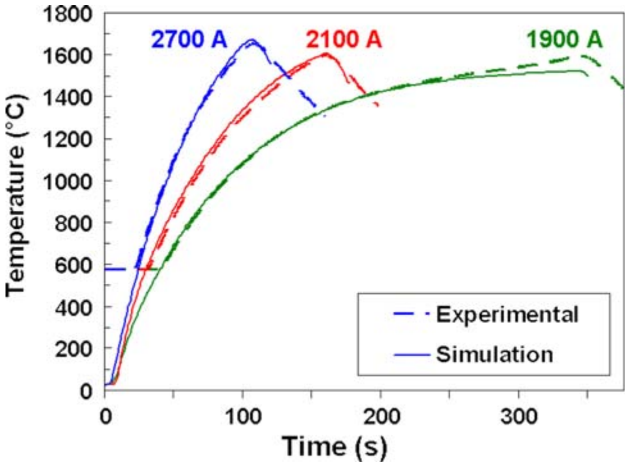

Fig. 20 Measured and predicted temperature versus time for 1,900, 2,100, and 2,700 A

Accordingly, the designed methodology is considered to be successfully tested thereby, the constructed SPS model can be reliably used to either aid optimum experiments design, explore in detail the SPS contact/bulk multiphysics or to predict powder microstructure on sintering. The possibility to correlate WC microstructure with process parameters is illustrated in detail elsewhere [16].

Understanding of SPS multiphysics

In this section, the validated SPS model is applied to elucidate SPS electrothermal–shrinkage phenomena in case of UF binderless WC powder sample.

The results above show that, although the WC powder volume is relatively small (2.8%) compared to that of the punch/die assembly, its bulk changes may induce dramatic changes in the overall current distribution with direct consequences on heat generation and temperature distribution. On the other hand, graphite elements mainly control the heating of the sample through their contact interfaces.

Figures 21a, b show the isothermal maps in the overall system after 40 and 153 s for 2,100 A. Such figures clearly confirm that in SPS-CCm process the punch/spacer interfaces experience the highest temperature peak in the system initially due to macro–constriction phenomena. The upper and lower spacers work as formidable heat sinks with respect to the hot punch. A large amount of heat is conducted from both interfaces towards both graphite spacers, thus, shifting the temperature peak to punch core. At the early transient, only a small amount of heat is conducted to the powder, whereas an even smaller amount is conducted to the die. At later time, the system heating is controlled by the minimum resistance among the powder, R_4 and R_2 contact resistances. Due to the initial dominance of R_2, most of the punches' heat flows to the powder system.

With the progress of heating, the thermal expansion effects become significant. R_2 contact resistance is large at the beginning and decreases (Fig. 15) with increasing time because of: (a) increased radial contact pressure induced by differential thermal expansion and (b) incipient powder densification. The peak temperatures decrease further during heating at all interfaces. As graphite parts become

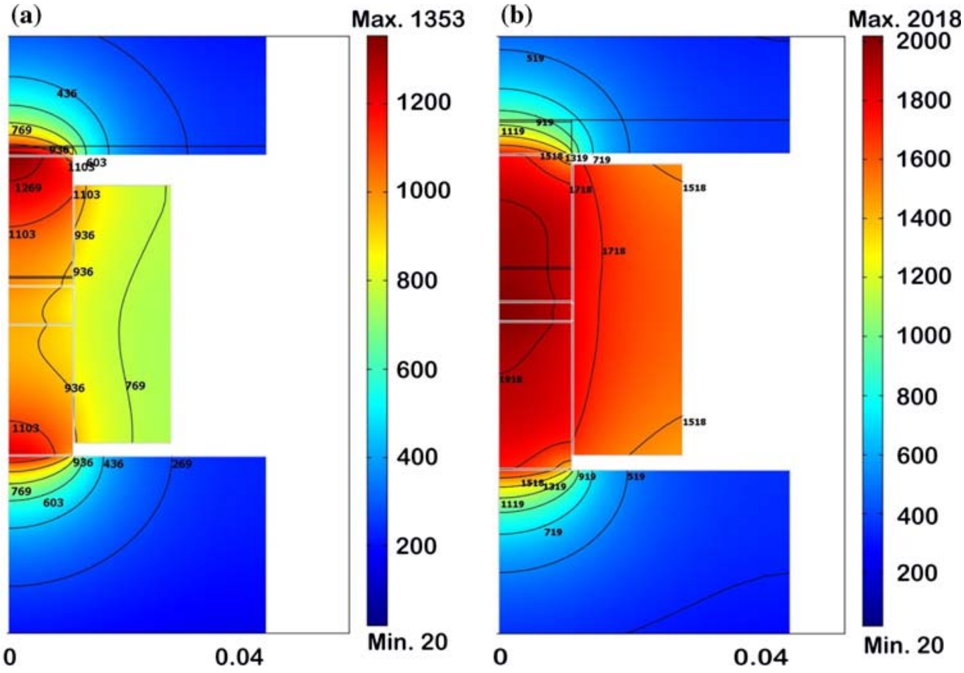

Fig. 21 Isothermal maps in °C for 2,100 A after **a** 40 s and **b** 153 s

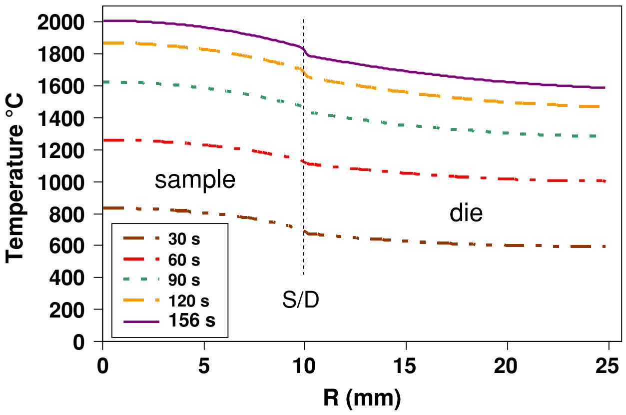

Fig. 22 Temperature versus radius (at powder mid-thickness plane) for 2,100 A and different heating times. S/D = sample/die interface

hotter, thermal radiation losses increase. The irradiated heat from punch outer surface is relatively small at the beginning, due to its small lateral surface, whereas that from the spacers' outer surface is much larger. Radiation losses from die outer surface are fair at the beginning but become increasingly larger with the progress of heating. At the end of sintering, the die is the major dissipation source of radiation of the SPS system. As a result, significant thermal gradients may develop along the die/sample assembly radius thereby, undesired microstructure and properties gradients may originate across the sample [16].

Figure 22 depicts the temperature distribution along the radius taking into account the die surface losses. It is well known that radiation losses are important at high temperatures. They, however, are not the only cause of thermal gradient development. For instance, radial thermal gradients may also develop when high heating rates are promoted in the SPS system (e.g., by high current input). In the latter case, electrothermal phenomena would be strongly controlled by contact resistances. The temperature profiles of Fig. 22 exhibit temperature jumps at the sample/die interface (S/D in figure), although their amplitude is lower than that at the punch/die interface at any time. The latter may range from about 40 °C, after 40 s, to about 100 °C, at the end of heating (i.e., 156 s) for 2,100 A (see also Fig. 21a, b). From Fig. 22, the heating rate at any point along the radius can be readily estimated.

Figure 23 shows the total current isopleths together with thermal fluxes (arrows) for 2,100 A after 156 s. At the end of sintering, the total currents mainly flow from the punches to the larger graphite spacers across the punch/spacer interfaces. This also applies for the thermal fluxes. The heat fluxes are largest at the punch/spacer interfaces due to the small contact surface areas [8]. A relatively larger heat flux is also observed at the punch/powder interface, thus, promoting heat flow towards the die. At this time, the powder is remarkably cooled down by conduction by the die.

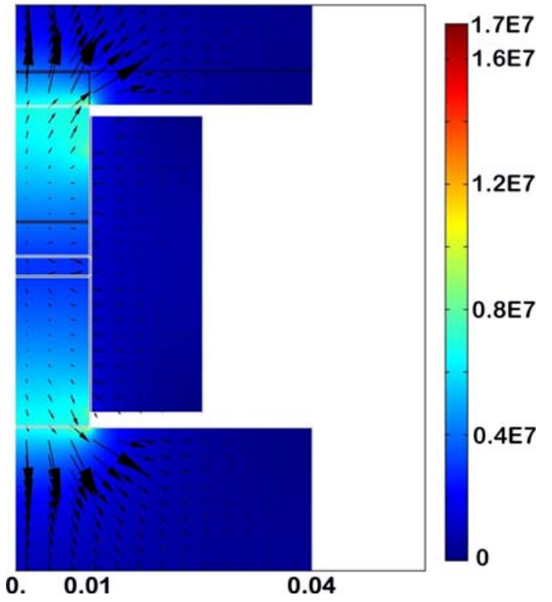

Fig. 23 Current density isopleth map (A/m^2) and heat flux (*arrows*) in W/m^2 for 2,100 A, after 156 s

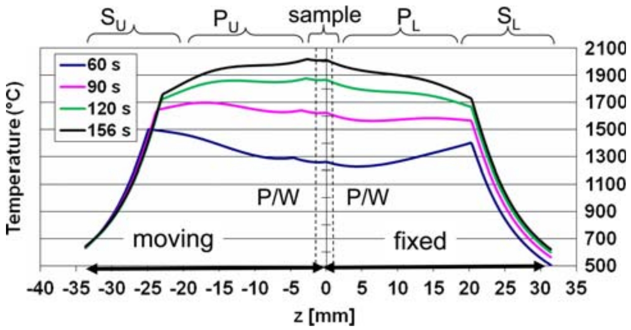

Fig. 24 Temperature versus z axial distance ($r = 0$) for 2,100 A for different sintering times. Symbols: P/S = punch/spacer interface; subscripts: U = upper; L = lower; P = punch; P/W = punch/WC interface. The (r,z) origin corresponds to intersection of symmetry axes with the horizontal axis located at the sample mid-thickness

It can be instructive to inspect the thermal gradients behavior along the axial direction. Figure 24 shows the temperature profiles for 2,100 A at various heating times. The negative z-axis (left) corresponds to the upper (moving) parts of the SPS system; vice versa the positive z-axis (right) corresponds to the lower (fixed) parts. This figure clearly shows the effect of the moving mesh on punch and spacer energetics, together with that on the sample along its thickness. The differences between the moving (left) and the fixed (right) parts are readily apparent. The moving mesh progressively modifies the SPS apparatus geometry symmetry. The punch sliding and the inherent contact resistance change cause a distortion of temperature profiles. These effects are not accounted in previous SPS models or calibration studies [2–15]. The upper temperature profiles are non-symmetric due to the upper punch movement. This implies a loss of geometry symmetry. Note, however, that as the P load is only applied to the upper part of the SPS system, there is no loading symmetry in the modeled SPS system. As a result, the computed fields are different in the upper and lower parts. The moving part accounts for higher temperatures compared to the fixed part. As the temperature at the punch/spacer interface is highest at the beginning, the punches core becomes relatively hotter. Only at the end of the cycle (156 s), the powder is heated up severely reaching the highest temperature in the system (above 1,900 °C).

The non-perfect contact between the inner die wall and the punch makes there the contact resistance very high especially at the beginning of sintering. The punch sliding contributes to conduct heat toward the die and the powder. By increasing the heating rate (or current input) the heating is more localized around the punch/spacer contact region. As the punch starts to slide, more heat is conducted into the die and the sample. However, the temperature may remain the maximum at the contact interfaces (not shown).

Note that, such non-symmetric heating would not happen if both the lower and the upper SPS parts were moving simultaneously or were fixed. Besides, the most important contribution accounted by the SPS model with punch sliding is the heating transient, which may be rather different compared to that described by motionless-punch SPS models. This proves why reliable SPS models have to take into account the sliding of punch to reliably predict the overall SPS energetics along with shrinkage conditions.

Finally, a detailed understanding of SPS shrinkage phenomena requires an accurate knowledge of field conditions in the sample. The electric field is the primary cause of heat generation and distribution in both the equipment and the powder. A priori it is not possible to explain the densification behavior of WC powder just by observing the die temperature. A proof of this is given by Fig. 25, which shows the predicted and measured displacement as a function of temperature for 2,100 and 2,700 A, respectively. Both the red (+) and black (solid) lines refer to predicted displacement inside the powder (i.e., shrinkage) as a function of predicted temperatures, whereas both, the blue (Δ) and cyan (□) lines, refer to measured punch displacement as a function of measured die surface temperature. The predicted shrinkage curves, for 2,100 and 2,700 A, respectively, take into account the differential thermal expansion effect of the system parts.

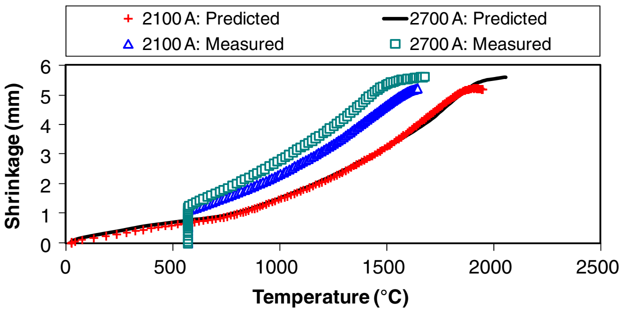

Fig. 25 Measured punch displacement and predicted shrinkage versus die surface temperature for 2,100 and 2,700 A in WC powder

The approximate overlapping of the simulated WC shrinkage curves, for 2,100 and 2,700 A, shows that the temperature dependence of shrinkage phenomena is the same for the two imposed currents, under the same powder and operating conditions. On the other hand, the experimental curves for both same imposed currents show a deviation between each other and a large deviation between them and the predicted curves. This explains as in general the die surface temperature measurements cannot help neither in monitoring the SPS shrinkage behavior nor in establishing a reliable correlation between microstructure and measured die surface temperature. Actually, the latter may lead to controversial results.

Recently published results [16] show that densification behavior, microstructure, and hardness can be reliably correlated with sintering temperature in WC powder with the aid of a thoroughly tested SPS model. Combined experiments and simulations by means of the proposed methodology show that sample microstructure and hardness are strongly functions of temperature field and heating rate.

Indeed, heating rate is another important factor, which may significantly influence the sample sintering behavior, although it may induce both non-uniform heating in the system parts and microstructure gradients [16]. In SPS-CCm process, heating rate increases with increasing imposed current. High currents, however, makes the SPS process difficult to control since heating rates may hold very high even in the last stage of sintering.

Figure 26 explores in detail the effect of heating rate along with the temperature difference between the powder core (predicted) and die surface (measured) for the three imposed currents (i.e., 1,900, 2,100, and 2,700 A). This figure confirms that at early times the temperature peaks in the system arise from contact interfaces. At the beginning, the electric contact resistance at the powder interface is higher, consequently the powder temperature increases more rapidly. As the contact resistances decrease also the powder temperature decreases and so it does the temperature difference between the powder and the die. Such a situation is displayed by the 1,900 A curve at about 50 s. At low and moderate temperatures, the overall temperature difference (between the sample core and the die surface) increases with increasing heating rate or current input. Vice versa, it decreases as heating rate decreases (or time increases) at higher temperatures even if thermal radiation

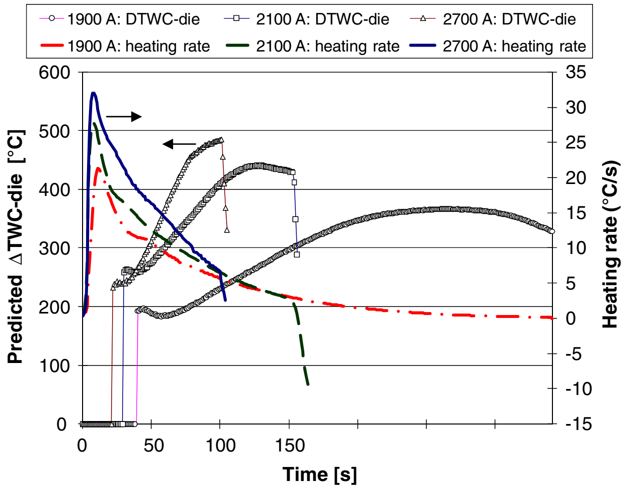

Fig. 26 Temperature difference between the WC core (predicted) and die surface (measured) along with predicted heating rate versus time for 1,900, 2,100, and 2,700 A

losses are significant. As a matter of fact, as heating rate decreases the temperature field exhibits smaller thermal gradients in the system. Consequently, the temperature difference tends to be constant or to decrease. By comparing the temperature difference behavior for the three imposed currents, we observe that the curve for the 2,700 A starts to increase earlier than those at 1,900 and 2,100 A because the punch is heated while moving, whereas the experimental temperature is measured on a fixed part.

From all considerations above, we are now in the condition to provide a more definite picture on the role of contact resistances in SPS.

The validation and calibration tests confirm the dominant role of vertical contact resistances in the control of heat generation and distribution in comparison to horizontal ones. Figures 19, 20 show an excellent fitting between experimental and numerical results in terms of voltage and temperature. In the calibration stages, special attention is paid to the tuning of R_1, R_2, R_4, since they significantly affect the fitting between experimental and numerical results. Even a small change of one of these contact resistances is able to dramatically change the current and temperature fields in the SPS system. Other contact resistances comparatively play a minor role but their tuning improves the reliability of the overall SPS model. R_1 is satisfactorily modeled by contact Joule's effect (i.e., thermoelectric coupling). R_2 and R_4 are effectively modeled by the moving boundary and the moving mesh kinematics. The decrease of R_2 while temperature increases (Fig. 15) is explained by two factors, namely the radial differential thermal expansion and powder shrinkage. The former factor is important when thermal gradients are relatively large. In SPS-CCm process, one typical origin for such occurrence is the large current input. In the present case, the contact resistance may even hold constant at any local temperature for 2,700 A. On the other hand, it decreases with increasing temperature for 2,100 A. In addition, the vertical contact resistivity are found to be independent of the displacement field, since the calibration procedure can be successfully performed by ignoring the densification behavior.

Finally, densification increases with increasing contact pressure, since it makes the contact surfaces tighter thereby more conductive.

The powder shrinkage resistance factor is actually a competing factor. The contact area at the powder/die interface decreases with the progress of shrinkage, thereby increasing R_4. On the other hand, the bulk powder resistance decreases due to an improved contact among powder particles. The latter contribution becomes more important after the early stage of sintering.

The nature and behavior of horizontal contact resistances is completely different from that of vertical contact resistances. They are usually subjected to the applied (constant) operating pressure. The latter is usually selected such that it just assures a good contact along horizontal interfaces during the whole sintering process. Thus, their contribution is minimal during SPS.

A final consideration concerns the values themselves of the estimated contact resistances in comparison to other works' findings. The final thermal and electric contact resistances estimated here are of the same order of magnitude of those predicted in [8, 10]. However, the temperature dependence of contact resistances found here differs from that of [8, 10], since the present calibration and validation procedures: (a) apply also to powders rather than only compact samples; (b) take into account the punch sliding effect. Nevertheless, the dependence of horizontal contact conductances on temperature found here is coherent with the model adopted in reference [8].

Conclusions

A numerical/experimental methodology is developed to build and thoroughly test a self-consistent SPS model. Experiments and simulations are carried out in current control mode (SPS-CCm). The SPS-CCm process offers an effective opportunity to directly compare SPS model outputs, such as current, temperature, and shrinkage with corresponding SPS recorded data. In addition, it allows exploring more systematically the effect of heating rates on sintering. The designed calibration/validation methodology coupled with the moving boundary/moving mesh-based SPS model allow for accurately accounting the overall SPS system energetics during sintering of UF binderless WC powder. This permits to make quantitative predictions or to design optimum experiments. Calibration and simulation tests show that the SPS process is particularly sensitive to R_1, R_2, R_4 contact resistances. Therefore, the reliability or the prediction capability of a SPS model strongly depends on their estimate accuracy. The results obtained can be used as a reference to benchmark different SPS systems or conditions, especially from the viewpoint of their contact resistances. A separated work demonstrates that a correlation between the final microstructure, the sintering temperature, the SPS parameters and the mechanical properties can be also established using the developed methodology. Although it has been tested on a simple geometry (i.e., disk) using conductive samples it may also apply to more complex geometries and insulating samples. Thus, the developed SPS model can be used as an aiding tool to either understand the bulk/contact multiphysics of SPS or to speed up set up time of the process as well as to design SPS experiments, which are of paramount importance for understanding SPS micro/macro phenomena.

Acknowledgements This work was supported by World Premier International Research Center Initiative (WPI Initiative), MEXT, Japan.

References

1. Munir ZA, Anselmi-Tamburini U, Ohyanagi M (2006) J Mater Sci 41:763. doi:10.1007/s1085-006-6555-2
2. Keum YT, Jeon JH, Auh KH (2002) J Ceram Proc Res 3:195
3. Leuenberger G, Ludwig R, Apelian D (2002) J Non-Destr Eval 21:111
4. Zhang J, Zavaliangos A, Kraemer M, Groza JR (2002) In: Lawley A, Smugeresky JE, Smith L (eds) Process modeling in powder metallurgy and particulate materials: Proceedings of the 2002 international conference on process modeling powder metallurgy and particulate materials, Newport Beach, CA, pp 208–215, 28–29 October 2002
5. Zhang J, Zavaliangos A, Groza JR (2003) In: International conference on powder metallurgy and particulate materials, Las Vegas
6. Zhang J, Zavaliangos A, Groza JR (2003) In: Cornwall RG, German RM, Messing GL (eds) Proceedings of sintering 2003, Materials Research Institute, Pennsylvania State University, University Park, PA, 14–17 September 2003
7. Zhang J, Zavaliangos A, Groza JR (2003) P/M Sci Tech Briefs 5:5
8. Zhang J (2003) Numerical simulation of sintering under electric field. PhD Thesis, Drexel University, Philadelphia, PA
9. Anselmi-Tamburini U, Garay JE, Munir ZA, Tacca A, Maglia F, Spinolo G (2004) J Mater Res 19:3255
10. Zavaliangos A, Zhang J, Krammer M, Groza JR (2004) Mater Sci Eng A 379:218
11. Anselmi-Tamburini U, Gennari S, Garay JE, Munir ZA (2005) Mater Sci Eng A394:139
12. Anselmi-Tamburini U, Garay JE, Munir ZA (2005) Mater Sci Eng. A 407:24
13. Vanmeensel K, Laptev A, Hennicke J, Vleugels J, Van der Biest O (2005) Acta Mater 53:4379
14. Cincotti A, Locci AM, Orru' R, Cao G (2007) AIChE J 53:703
15. Olevsky E, Froyen L (2006) Scr Mater 55:1175
16. Maizza G, Grasso S, Sakka Y, Noda T, Ohashi O (2007) Sci Tech Adv Mater 8:644
17. COMSOL Multiphyscs (2006) AC/DC Module, User's Guide Vers.3.3a, August
18. Savvatimskiy AI (2005) Carbon 43:1115
19. Loeb AL (1954) J Am Ceram Soc 37:96
20. Austin JB (1941) Ceram Abstr 20:45
21. Sahimi M, Tsotsis TT (1999) Ind Eng Chem Res 36:3043
22. Willims WS (1998) JOM 50:62
23. Reeber RR, Wang K 1999) J Am Ceram Soc 82:129
24. Toyo Tanso Co. Ltd. Tokyo private communication
25. Holm R (1967) Electric contacts: theory and application. Springer, New York
26. Nishimoto K, Saida K, Tsuduki R (2001) J Jpn Inst Met 65:747
27. Luo X, Chung DDL (2001) J Tribol 123:683
28. Xie G, Ohashi O, Yamaguchi N, Wang A (2003) Metall Mater Trans A 34:2655
29. Bahrami M, Culham JR, Yovanovich MM (2004) J Heat Transf 126:896
30. Bahrami M, Culham JR, Yovanovich MM, Schneider GE (2004) J Thermophys Heat Transf 18:218
31. Song Q, Zhang W, Niel B (2005) Weld J 84:73